



Frequency modulation of body waves to improve performance of sidewinding robots

The International Journal of
Robotics Research
1–16
© The Author(s) 2021
Article reuse guidelines:
sagepub.com/journals-permissions
DOI: 10.1177/02783649211037715
journals.sagepub.com/home/ijr
 SAGE

Baxi Chong^{1*} , Tianyu Wang^{1*} , Jennifer M. Rieser², Bo Lin¹ ,
Abdul Kaba³, Grigoriy Blekherman¹, Howie Choset⁴ and Daniel I. Goldman¹

Abstract

Sidewinding is a form of locomotion executed by certain snakes and has been reconstructed in limbless robots; the gait is beneficial because it is effective in diverse terrestrial environments. Sidewinding gaits are generated by coordination of horizontal and vertical traveling waves of body undulation: the horizontal wave largely sets the direction of sidewinding with respect to the body frame while the vertical traveling wave largely determines the contact pattern between the body and the environment. When the locomotor's center of mass leaves the supporting polygon formed by the contact pattern, undesirable locomotor behaviors (such as unwanted turning or unstable oscillation of the body) can occur. In this article, we develop an approach to generate desired translation and turning by modulating the vertical wave. These modulations alter the distribution of body–environment contact patches and can stabilize configurations that were previously statically unstable. The approach first identifies the spatial frequency of the vertical wave that statically stabilizes the locomotor for a given horizontal wave. Then, using geometric mechanics tools, we design the coordination between body waves that produces the desired translation or rotation. We demonstrate the effectiveness of our technique in numerical simulations and on experiments with a 16-joint limbless robot locomoting on flat hard ground. Our scheme broadens the range of movements and behaviors accessible to sidewinding locomotors at low speeds, which can lead to limbless systems capable of traversing diverse terrain stably and/or rapidly.

Keywords

bio-inspired robot, limbless locomotion, geometric mechanics

1. Introduction

Biological limbless locomotors successfully maneuver over complex terrain, partially because of their ability to regulate contact between their bodies and the environment (Astley et al., 2015; Gong et al., 2015; Hu et al., 2009; Jayne, 1986; Marvi et al., 2014). Of specific interest to our work, sidewinding motion offers an excellent example of the importance of contact pattern regulation. In sidewinding motion, some portions of body are cyclically lifted from the ground, which we refer to as *vertical wave*, in coordination with the undulatory motion in the horizontal plane, which we refer to as *horizontal wave*. Proper coordination of these waves can generate self-propulsive forces that cause motions in a desired direction, thereby enabling high maneuverability in sidewinding locomotion (Astley et al., 2015; Gong et al., 2015; Hu et al., 2009; Marvi et al., 2014).

Despite the maneuverability benefits of sidewinding, if not properly coordinated, lifting certain body segments can often result in unstable configurations: the locomotor's

center of mass (CoM) can leave the support polygon formed by body contacts (McGehee and Iswandhi, 1979). Such a situation can result in the loss of body configuration stability, which we refer to as static stability. This loss of static stability could be compensated for by dynamic stability when operating at high speed, such that the duration of the unstable configuration is too short to affect the robot's overall dynamics (McGeer, 1990). In contrast, at low speed, the loss of static stability can lead to unexpected body contacts

¹Georgia Institute of Technology, Atlanta, GA, USA

²Emory University, Atlanta, GA, USA

³Morehouse College, Atlanta, GA, USA

⁴Carnegie Mellon University, Pittsburgh, PA, USA

*These authors contributed equally.

Corresponding author:

Baxi Chong, Complex Rheology and Biomechanics Laboratory, Howey Physics Building, 837 State Street NW, Atlanta, GA 30332, USA.
Email: bchong9@gatech.edu

and change the ground reaction force distribution, which can lead to undesirable deviations from the target behaviors.

While modulation of the horizontal wave could lead to stable gaits, such stabilization often comes with the cost of lower speed and/or changes in the direction of motion (Astley et al., 2015, 2020). Therefore, it is preferable to stabilize gaits by modulating the vertical waves. Marvi et al. (2014) demonstrated that on granular media, modulating the amplitude of waves in the vertical plane can increase the amount of the body in contact with the environment and, therefore, improve the robustness of gaits on sandy slopes. In contrast, on non-deformable flat ground or even on rough terrain, the contact distribution is less dependent on amplitude modulation. Therefore, there is a need to stabilize gaits by other modulations.

Inspired by contact planning methods in legged robots (Ijspeert et al., 2007; Li et al., 2009; Pongas et al., 2007; Ponton et al., 2020), we propose an approach to stabilize statically unstable gaits by modulating the body contact pattern. However, unlike legged robots, where contact patterns can be readily realized and implemented, it is challenging to modulate the contact pattern for serial limbless robots, partially because the contact states of modules in serial limbless robots are not independently modulated like those in legged robots. Another challenge lies in the fact that modulation in body contact pattern not only provides additional stability but also alters the distribution of ground contact forces and, hence, the direction of motion (Astley et al., 2015).

In this article, we develop an approach to stabilize statically unstable sidwinding gaits. We employ a 3D configuration optimization scheme (Wang et al., 2021) which calculates the robot's joint angles to realize a desired contact pattern. We show that the generated contact patterns can be accurately implemented on robots, which allows us to redesign the contact pattern and therefore stabilize the gaits. We then apply geometric mechanics tools (Gong et al., 2018; Hatton and Choset, 2015; Hatton et al., 2013; Marsden and Ratiu, 2013) to coordinate motions in the horizontal plane and the contact pattern, which leads to translation and rotation in a chosen direction. As a result, we extend the sidwinding gait family and obtain effective and statically stable sidwinding gaits in both translation and rotational movements. We validate our theoretical predictions by numerical simulation (Figure 1(a)) and experiments with a 16-joint serial elastic actuated (SEA) limbless robot (Figure 1(b)) locomoting on flat hard ground.

2. Related work and methods

2.1. Sidwinder locomotion

Biological sidwinding motion has been described as the superposition of two traveling waves: one in the horizontal plane and another in the vertical plane (Astley et al., 2015; Marvi et al., 2014; Rieser et al., 2019). The horizontal wave of body curvature is described by

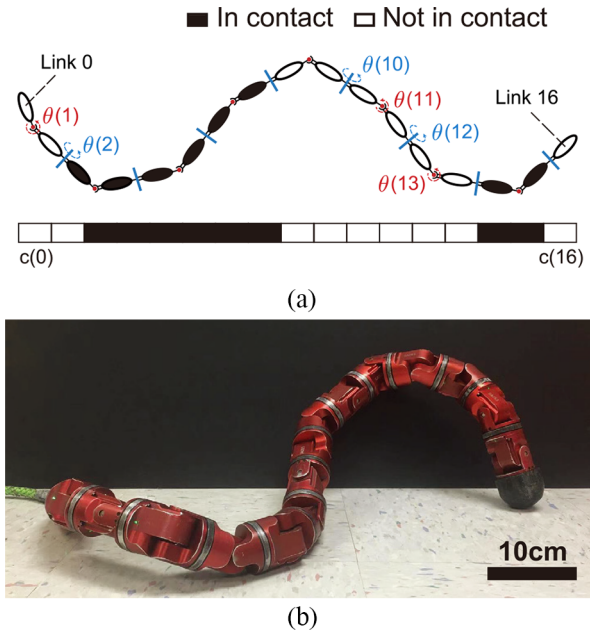


Fig. 1. Theoretical model and experimental robot. (a) The theoretical model for the sidwinder robots. The filled black ovals indicate the ground contact phase whereas the white ovals indicate a no ground contact phase. The contact state is labeled in black ($c(i)$). The joint angle in blue indicates pitch joints and the joint angle in red indicates yaw joints. (b) The SEA robot used to test the effectiveness of our stabilization approach.

$$\kappa(s, t) = \kappa_m \sin(\omega_t t + \omega_s s) \quad (1)$$

where $s \in [0, 1]$ indicates the position along the arc length of the body ($s=0$ denotes head and $s=1$ denotes tail); $\kappa(s, t)$ denotes the local body curvature at position s and time t ; κ_m , ω_s , and ω_t denote the amplitude, the spatial frequency, and the temporal frequency of body curvatures, respectively.

The vertical wave is often reconstructed as a time-dependent contact state:

$$c(s, t) = \sigma[\sin(\omega_s t + \omega_s s + \phi_0)] \quad (2)$$

where $\sigma[x] = \frac{1}{1+e^{-\gamma x}}$, with the parameter γ approximating the sharpness of the contact state transition; and ϕ_0 is the phase difference between the horizontal wave and the vertical wave. Note that $\gamma \rightarrow \infty$ indicates a stepwise transition in contact state; to allow the continuity and the differentiability in (2), we take $\gamma=4$ in this article unless otherwise stated. Previous work (Astley et al., 2015) revealed that $\phi_0 = \pm\pi/2$ yields to effective sidwinding motion.

Our group has demonstrated aspects of the performance of sidwinding snakes in robots (Astley et al., 2015, 2020; Gong et al., 2015; Hatton and Choset, 2010). In our experiments, we use limbless robots with adjacent rotary motors rotated by 90° such that successive modules can achieve rotation in the horizontal and vertical planes alternatively. In this way, the robot can have 3D configurations by a superposition of a vertical wave and a horizontal wave. For

an N -joint limbless robot, joints are labeled 1 to N , and links are labeled from 0 to N , where joint j connects link $j - 1$ and link j . Odd numbered joints are *yaw* joints and therefore produce motion in the horizontal plane (their rotation axes are vertical). Even numbered joints are *pitch* joints and, therefore, produce motion in the vertical plane (their rotation axes are horizontal). The joint angles are prescribed using the following functions:

$$\theta(2j - 1, t) = A_l \sin\left(2\pi K_l \frac{2j - 1}{N} + 2\pi ft\right) \quad (3)$$

$$\theta(2j, t) = A_v \sin\left(2\pi K_v \frac{2j}{N} + 2\pi ft + \phi_0\right) \quad (4)$$

where $\theta_l(2j - 1, t)$ and $\theta_v(2j, t)$ refer to the yaw (odd) joint angles and the pitch (even) joint angles, respectively; K_l and K_v are the spatial frequency of the horizontal wave and the vertical wave, respectively; A_l and A_v are the amplitude of the horizontal wave and the vertical wave, respectively; f defines the temporal frequency; and ϕ_0 is the phase lag between the horizontal and the vertical wave.

The contact state of link i is represented by $c(i)$, where $c(i) = 1$ indicates that link i is in contact and $c(i) = 0$ indicates that link i is not in contact. The links between two consecutive vertical joints have the same contact state, i.e., $c(2j) = c(2j - 1)$. Therefore, the contact state in robots can be approximated by (Rieser et al., 2019)

$$\begin{aligned} c(2j - 1, t) &= c(2j, t) \\ &= \sigma \left[\sin\left(2\pi K_v \frac{j}{2N} + 2\pi ft + \phi_0\right) \right] \end{aligned} \quad (5)$$

Previous work (Burdick et al., 1993) demonstrated that some combinations of gait parameters (specifically, $K_l = K_v$ and $\phi_0 = \pm\pi/2$) can lead to translational sidewinding (which we refer to as “T-sidewinding”) motion, where the locomotor displays translational displacement with no significant turning. Note that during conventional sidewinding ($K_l = K_v$ and $\phi_0 = \pm\pi/2$), the direction of motion is always 90° with respect to body axis regardless of the horizontal amplitude. However, the modulation of horizontal amplitude can affect the orientation of the “tracks” left by body contacts (the track angle (Rieser et al., 2019)).

In addition, the modulation of the horizontal wave has been shown to enable high maneuverability in sidewinding locomotion. Astley et al. (2020) and Rieser et al. (2019) showed that the direction of translation (the angle between the direction of motion and the body axis) can be modulated by controlling A_l . Moreover, introducing differential horizontal wave amplitude from head to tail results in gradual rotation in limbless robot (Astley et al., 2015). In addition to the modulation in the horizontal wave, Marvi et al. (2014) showed that manipulation of the vertical amplitude A_v can change the body contact ratio (average percentage of the body that is in contact with the environment), and therefore enable climbing on sandy slopes. Finally, modulating

Table 1. Summary of previous work on sidewinder locomotion

K_l	K_v	ϕ_0	Behavior	Source
1.5	1.5	$\pi/2$	T-sidewinding	Marvi et al. (2014)
2	2	$\pi/2$	T-sidewinding	Astley et al. (2015)
1.5	0.9	$\pi/2$	R-sidewinding	Astley et al. (2015)
1.5	1.95	$\pi/2$	R-sidewinding	Astley et al. (2015)
1.5	3	0	Slithering	Hu et al. (2009)

the ratio of the spatial frequency in the vertical and horizontal directions (K_v/K_l) yields turning gaits (*frequency turning* in Astley et al. (2015)). Either increasing ($K_v = 1.3K_l$) or decreasing ($K_v = 0.6K_l$) the vertical spatial frequency will lead to clockwise (CW) turning. In this article, we refer the frequency turning as the rotational sidewinding (which we refer to as “R-sidewinding”) motion. Beyond sidewinding, the sinus lifting gait is another snake gait uses horizontal and vertical wave. Hu et al. (2009) showed that snakes lift body portions with the largest curvatures during lateral undulation (slithering) locomotion. In the scheme defined in (3) and (5), this form of locomotion has $K_v = 2K_l$ and $\phi_0 = 0$. We summarize previous work on wave modulation in Table 1.

2.2. Contact pattern realization

For 3D limbless robots, sidewinding locomotion is composed of a continuous sequence of 3D configurations. Each 3D configuration is a “sum” of a 2D configuration in the horizontal plane and a 2D configuration in the vertical plane (Astley et al., 2015). Ideally, the projections of the 3D configuration onto the horizontal and vertical planes are identical to the desired 2D horizontal configuration and the desired 2D vertical configuration. When fitting a mechanism to a backbone curve, three-degree-of-freedom joints are practically preferred since they are easier to capture pitch, roll and yaw. However, our snake robot, along with many others (Fu and Li, 2020; Rollinson et al., 2014; Takemori et al., 2018), only has pitch and yaw degrees of freedom (as shown in Figure 1(a)). If the robot’s yaw and pitch joints directly employ the horizontal and vertical joint angle equations (as (3)–(4)), the composed 3D configuration of the robot fails to capture the twist features in the desired 3D configuration (Wang et al., 2021). The inaccuracy of the 3D configuration can, in turn, cause an inaccurate contact pattern realization (CPR). Previous studies hypothesised that the vertical joint angle prescribed by (4) can lead to the contact pattern in (5) (Marvi et al., 2014; Rieser et al., 2019). Although in many cases such correspondence is reasonable, in some cases the discrepancy in the correspondence can lead to unexpected locomotion behavior. Therefore, we apply a 3D configuration optimization tool (Wang et al., 2021) to implement an accurate mapping from the desired contact pattern to the robot joint angles. In this section, we provide detailed steps to realize an arbitrary contact pattern.

2.2.1. Desired configuration generation. To achieve the desired configuration for an N -joint robot, we first denote the 3D Cartesian coordinates of the anterior endpoint of the robot by P_0 , the posterior endpoint of the robot by P_{N+1} , and N joints by P_1, P_2, \dots, P_N . We define the xy -plane as the horizontal plane and the xz -plane as the vertical plane.

We first obtain the coordinates of links in the xy -plane by iteratively solving $[P_{i,x}, P_{i,y}]^T$ by varying j from 0 to $N/2$ following

$$\begin{aligned} g \begin{pmatrix} P_{2j+1,x} \\ P_{2j+1,y} \\ P_{2j+1,\theta} \end{pmatrix} &= g \begin{pmatrix} P_{2j,x} \\ P_{2j,y} \\ P_{2j,\theta} \end{pmatrix} D \\ g \begin{pmatrix} P_{2j+2,x} \\ P_{2j+2,y} \\ P_{2j+2,\theta} \end{pmatrix} &= g \begin{pmatrix} P_{2j+1,x} \\ P_{2j+1,y} \\ P_{2j+1,\theta} \end{pmatrix} R(\theta(2j+1))D \end{aligned} \quad (6)$$

where

$$\begin{aligned} g \begin{pmatrix} x \\ y \\ \theta \end{pmatrix} &= \begin{bmatrix} \cos(\theta) & -\sin(\theta) & x \\ \sin(\theta) & \cos(\theta) & y \\ 0 & 0 & 1 \end{bmatrix} \\ D &= \begin{bmatrix} 1 & 0 & L \\ 0 & 1 & 0 \\ 0 & 0 & 1 \end{bmatrix} \\ R(\theta) &= \begin{bmatrix} \cos \theta & -\sin \theta & 0 \\ \sin \theta & \cos \theta & 0 \\ 0 & 0 & 1 \end{bmatrix} \end{aligned}$$

$\theta(2j-1)$ is the yaw joint angle defined in (3); $P_{i,\theta}$ is a dummy variable introduced to obtain the coordinates (with initial condition defined as $P_{0,\theta} = 0$); and L is the link length.

Next, we obtain the coordinates in the xz -plane:

$$P_{i,z} = \left(1 - c\left(i - \frac{1}{2}\right)\right)h \quad (7)$$

where $c\left(i - \frac{1}{2}\right)$ is the contact state of joint i (we use $i - \frac{1}{2}$ to indicate the relative position of joint i which connects link $i-1$ and link i along the body) defined in (2), and h is amplitude of body lifting, which we empirically relate to A_v by $\sin(A_v) = h/L$. Note that under (7), the contact pattern is realized by lifting the modules not in contact with the ground by h .

Finally, we performed a 3D spline fitting to the discrete coordinates P_0, \dots, P_{N+1} to achieve a continuous curve. We then uniformly resample the curve with $N+2$ sample points P_0', \dots, P_{N+1}' such that distances between any two consecutive points P_i' and P_{i+1}' are equal, i.e., if we denote the $N+1$ links by vectors $l_i = P_{i+1}' - P_i'$ for $0 \leq i \leq N$, all l_i have the identical length.

2.2.2. Robot joint position optimization. We use $N+2$ coordinates Q_0, Q_1, \dots, Q_{N+1} to denote the optimized

positions for the anterior endpoint of the robot, N joints of the robot, and the posterior endpoint of the robot. Thus, the optimal robot configuration (which is as close to the desired configuration as possible) is found by minimizing the objective function

$$\sum_{i=0}^{N+1} \|P_i' - Q_i\|^2 \quad (8)$$

We denote the $N+1$ links in the optimized robot configuration by vectors $l_i' = Q_{i+1} - Q_i$ for $0 \leq i \leq N$. As each joint possesses a single rotational degree of freedom, the two links l_{i-1}' and l_i' at joint i should lie in the same rotational plane α_i ($1 \leq i \leq N$). We associate a unit normal vector $n_i \in \mathbb{R}^3$ to plane α_i ($\|n_i\| = 1$) to describe its direction. The alternating pitch and yaw joints robot geometry draws the constraint that any two consecutive rotation planes should be orthogonal in \mathbb{R}^3 , yielding $n_i \cdot n_{i+1} = 0$, for all $1 \leq i \leq N-1$.

Given that the two links l_{i-1}' and l_i' both belong to the plane α_i and the normal vector n_i is orthogonal to α_i , n_i is orthogonal to both l_{i-1}' and l_i' . It follows that the three vectors l_{i-1}', n_i, n_{i-1} are pairwise orthogonal. In other words, l_{i-1}' is parallel to the cross product $n_{i-1} \times n_i$ for $2 \leq i \leq N$.

Assuming the internal shape of the robot is fixed, i.e., relative positions of all Q_i are determined, the value of the objective function will only depend on the choice of absolute positions of Q_i . We let $d_i = P_i' + (Q_0 - Q_i)$, where d_i are constants under the assumption, then the objective function can be expressed as

$$\begin{aligned} \sum_{i=0}^{N+1} \|P_i' - Q_i\|^2 &= \sum_{i=0}^{N+1} [(Q_0 - d_i) \cdot (Q_0 - d_i)] \\ &= \sum_{i=0}^{N+1} [Q_0 \cdot Q_0 - 2Q_0 \cdot d_i + d_i \cdot d_i] \\ &= (N+2)Q_0 \cdot Q_0 - 2Q_0 \cdot \left(\sum_{i=0}^{N+1} d_i\right) + \sum_{i=0}^{N+1} (d_i \cdot d_i) \\ &= (N+2) \left(Q_0 - \frac{\sum_{i=0}^{N+1} d_i}{N+2}\right) \cdot \left(Q_0 - \frac{\sum_{i=0}^{N+1} d_i}{N+2}\right) \\ &\quad + \left[\sum_{i=0}^{N+1} (d_i \cdot d_i) - \frac{1}{N+2} \left(\sum_{i=0}^{N+1} d_i\right) \cdot \left(\sum_{i=0}^{N+1} d_i\right)\right] \end{aligned}$$

Note that the last term in the square bracket is a constant. Thus, the objective function attains the minimum if and only if $Q_0 = \frac{1}{N+2} \sum_{i=0}^{N+1} d_i$, which is equivalent to $\sum_{i=0}^{N+1} Q_i = \sum_{i=0}^{N+1} P_i'$. Also note that this constraint is derived purely mathematically, but an intuitive interpretation of the constraint is that the centroid of the actual robot configuration should coincide with the centroid of the desired configuration.

We now arrive at the final formulation the optimization problem which exploits the geometric structure of the robot

$$\begin{aligned}
& \underset{Q_i}{\text{minimize}} && \sum_{i=0}^{N+1} \|P_i - Q_i\|^2 \\
& \text{subject to} && \text{(i) } \|n_i\| = 1, \forall 1 \leq i \leq N \\
& && \text{(ii) } n_i \cdot n_{i+1} = 0, \forall 1 \leq i \leq N-1 \\
& && \text{(iii) } l'_{i-1} = L \cdot (n_{i-1} \times n_i), \forall 2 \leq i \leq N \\
& && \text{(iv) } \sum_{i=0}^{N+1} Q_i - \sum_{i=0}^{N+1} P_i' = 0
\end{aligned}$$

The constrained nonlinear optimization problem can be solved by standard gradient-descent algorithms such as MATLAB's built-in function `fmincon` (MATLAB, 2020). For the sideward gaits we proposed in this work, we experimentally verified that solving the nonlinear optimization using MATLAB is feasible for the real-time implementation in the quasi-static motions. However, a limitation of this method is that optimization problems might not be solved fast enough in the scenarios where the robot has to execute the gaits with complex backbone curves under high temporal frequencies. In such cases, pre-optimizing the configurations offline should be considered.

2.2.3. Joint angle derivation. The optimization algorithm outputs the optimized coordinates $Q_0, Q_1, \dots, Q_{N+1} \in \mathbb{R}^3$, which denote the optimal positions for N joints, and the anterior and the posterior endpoints of the robot in the work-space. To implement the optimized robot configuration on the physical robot, we must translate the coordinates to the robot joint angles in joint space: the absolute value of the i th joint angle is achieved by the inner product of l'_i and l'_{i-1} , given the coordinates Q_0, Q_1, \dots, Q_{N+1} ; and the orientation of the i th joint angle can be determined by the direction of the normal vector n_i of the rotation plane α_i , given the coordinates Q_0, Q_1, \dots, Q_{N+1} .

Thus the optimized joint angles θ_i ($i = 1, \dots, N$) are sent to the robot as joint angle set points.

2.3. Geometric mechanics

In this subsection, we provide an overview of the geometric tool, which we use to design the coordination between the horizontal wave and the vertical wave to produce motions in our desired direction. For a more detailed and comprehensive review, we refer reader to Marsden and Ratiu (2013), Gong et al. (2018), Zhong et al. (2018), and Chong et al. (2019). The geometric mechanics gait design framework separates the configuration space of a system into two spaces: a position space and a shape space. The position space represents the location (position and rotation) of a system in the world frame, whereas the shape space denotes the internal shape of the system. The geometric mechanics framework then establishes a functional relationship to map the velocities in the shape space to the velocities in the position space; this functional relationship is often called a *local connection*.

2.3.1. Kinematic reconstruction equation. In kinematic systems where inertial effects are negligible, the equations of motion (Marsden and Ratiu, 2013) can often be approximated as

$$\xi = A(r)\dot{r} \quad (9)$$

where $\xi = [\xi_x, \xi_y, \xi_\theta]^T$ denotes the body velocity in the forward, lateral, and rotational directions; r denotes the internal shape variables (joint angles); $A(r)$ is the local connection matrix, which encodes environmental constraints and the conservation of momentum. As shown in Hatton et al. (2013), the local connection matrix, A , can be numerically derived by force and torque balance. It is challenging to model the ground reaction forces precisely, especially for a diverse contact surfaces. However, as shown in Rieser et al. (2019), modeling movement on hard ground using a speed-independent kinetic Coulomb friction force model has produced good agreement with experimental data.

2.3.2. Connection vector fields and height functions. Each row of the local connection matrix, A , corresponds to a component direction of the body velocity. Each row of the local connection matrix over the shape space then forms a connection vector field. In this way, the body velocities in the forward, lateral, and rotational directions are computed as the dot product of connection vector fields and the shape velocity \dot{r} .

The displacement along the gait path $\partial\phi$ can be obtained by integrating the ordinary differential equation (Hatton and Choset, 2015):

$$g(T) = \int_{\partial\phi} T_e L_{g(r)} A(r) dr \quad (10)$$

where $g(t) = [x(t), y(t), \alpha(t)]^T \in SE(2)$ represents the position and rotation of body frame viewed in the world frame (Murray, 2017); $g(T) = [\Delta x, \Delta y, \Delta\alpha]^T$ denotes the translation and rotation of the body frame (with respect to the world frame) in one gait cycle. Note that $T_e L_g$ is the left-lifted action with respect to the coordinates of g :

$$T_e L_g = \begin{bmatrix} \cos(\alpha) & -\sin(\alpha) & 0 \\ \sin(\alpha) & \cos(\alpha) & 0 \\ 0 & 0 & 1 \end{bmatrix}$$

The integral of (10) can be approximated to the first order by

$$\begin{pmatrix} \Delta x \\ \Delta y \\ \Delta\theta \end{pmatrix} = \int_{\partial\chi} A(r) dr \quad (11)$$

The accuracy of the approximation in (11) can be optimized by properly choosing the body frame (Hatton and Choset, 2015; Lin et al., 2020). According to Stokes' theorem, the line integral along a closed curve $\partial\chi$ is equal to the

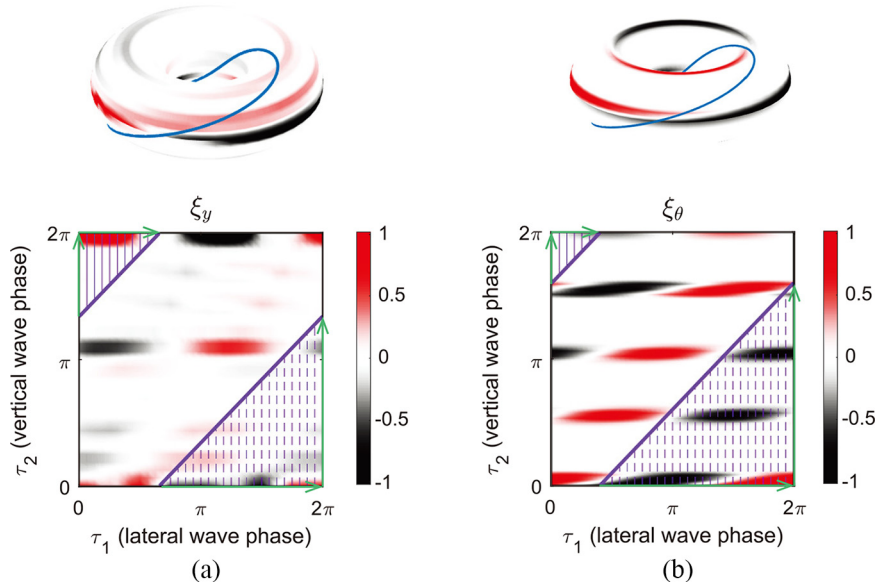


Fig. 2. Height functions to design gaits to produce motion in the desired direction. Height functions on torus (top panel) and on unfolded Euclidean cover space (lower panel) are shown. The height function for (a) horizontal spatial frequency $K_l = 1.5$, $V-L$ ratio $K_v/K_l = 1.3$ in lateral direction (the direction perpendicular to body axis) and (b) horizontal spatial frequency $K_l = 0.9$, $V-L$ ratio $K_v/K_l = 1.2$ in rotational direction. The purple curve in each plot maximizes the surface integral enclosed in the upper left corner (marked in solid lines) minus the surface integral enclosed in the lower left corner (marked in the dashed lines). The assistive lines are shown as lines with green arrows.

surface integral of the curl of $\mathbf{A}(\mathbf{r})$ over the surface enclosed by $\partial\chi$:

$$\int_{\partial\chi} \mathbf{A}(\mathbf{r}) d\mathbf{r} = \iint_{\chi} \nabla \times \mathbf{A}(\mathbf{r}) d\mathbf{r}_1 d\mathbf{r}_2 \quad (12)$$

where χ denotes the surface enclosed by $\partial\chi$. The curl of the connection vector field, $\nabla \times \mathbf{A}(\mathbf{r})$, is referred to as the height function (Hatton and Choset, 2015). The three rows of the vector field $\mathbf{A}(\mathbf{r})$ can, thus, produce three height functions in the forward, lateral, and rotational direction, respectively.

With the above derivation, we simplify the gait design problem to drawing a closed path in a Euclidean shape space. Displacements can be approximated by the integral of the surface enclosed by the gait path. Hence, maximizing the integral leads to the maximal displacement.

2.3.3. Toroidal shape space. As we discuss in detail in Section 3.1.4, in the sidewinding gait prescription, one of the shape variables represents the phase of the horizontal wave ($\tau_1 \in S^1$), and the other shape variable represents the phase of the vertical wave ($\tau_2 \in S^1$). With both shape variables being cyclic, its shape space is toroidal, (T^2) (Kobayashi and Nomizu, 1963). Examples of height functions on toroidal shape spaces are shown in Figure 2. Although the gait path (solid purple curve in Figure 2) is a closed curve in the toroidal shape space, there is no obvious surface enclosed by the gait path.

To form an enclosed surface, Gong et al. (2018) introduced the notion of “assistive lines” in the Euclidean cover space of the toroidal shape space. As a result, the surface integral can be calculated as the surface enclosed in the upper left corner (see the surface labeled by solid lines in Figure 2) minus the surface enclosed in the lower right corner (see the surface labeled by dashed lines in Figure 2). We refer reader to Gong et al. (2018) for a detailed derivation and proof of motion planning in toroidal shape spaces.

3. Frequency modulation to stabilize gaits

3.1. Sidewinder gait formula

3.1.1. Joint angle prescription. We prescribe the joint angle using two methods, sine wave prescription (SWP) and CPR. In SWP, we use (3) and (4) to directly prescribe the joint angle according to our choice of gait parameters. In CPR, we use the methods introduced in Section 2.2 to calculate the joint angles for our choice of gait parameters.

Note that in our robot (see Section 3.3 for a detailed description), joint N (the last joint) always orients link N (the tail link) into the air so the tether does not interfere with robot motion.

3.1.2. Static stability. Static stability is defined as the fraction of a temporal undulation period that the CoM is inside the support polygon. The support polygon is defined as the convex hull of all the links in contact with substrate. In Figure 3, we show examples of stable (Figure 3(a)) and

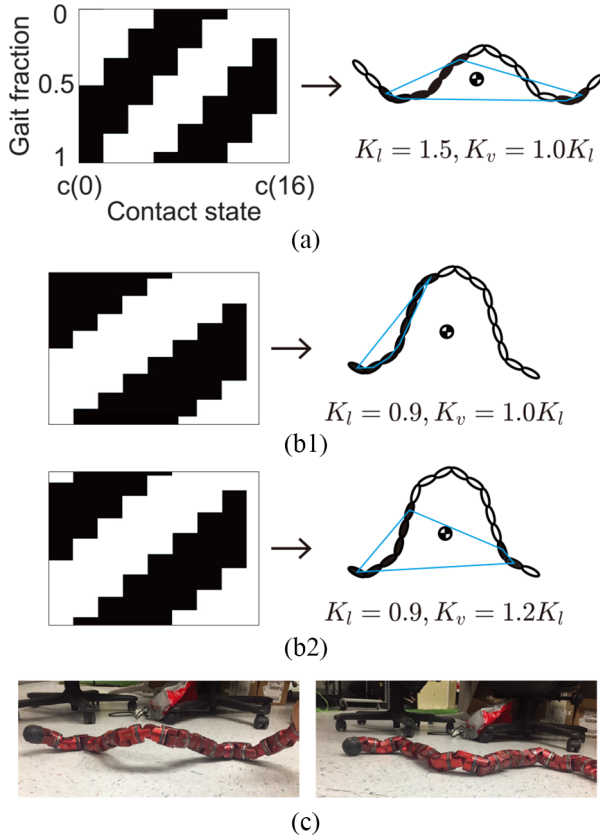


Fig. 3. Examples of statically stable and unstable configurations. (a) The contact state pattern and an example of a statically stable configuration for gaits with high spatial frequency in both the horizontal wave and the vertical wave. (b1) The contact state pattern and an example of a statically unstable configuration for gaits with low spatial frequency in both the horizontal wave and the vertical wave. (b2) Stabilizing the statically unstable configuration by increasing the vertical spatial frequency. The label and the axis in panel (b) are the same as in (a). (c) Example of an unstable configuration (left) and an unexpected touchdown (right)

unstable configurations (Figure 3(b)). We observe that gaits with large vertical spatial frequencies have more distinct body–environment contact patches, and are therefore more statically stable than gaits with low spatial frequency in the vertical wave. Inspired by this observation, we stabilize the originally unstable gaits by increasing the spatial frequencies of the vertical wave (*frequency modulation*).

3.1.3. Gait stabilization. We stabilize the sidewinding gaits by increasing the spatial frequency of the vertical wave. In other words, we gradually increase the V – L ratio, K_v/K_l , until the satisfactory static stability is reached. As we increase the vertical spatial frequency, the vertical spatial period decreases. Thus, lower vertical spatial frequency represents shorter but more frequent contact patterns, which is more stable; whereas higher vertical spatial frequency represents longer but less-frequent contact patterns, which

is less stable. In this article, we consider a gait as statically stable when its static stability is greater than 0.5. Note that this threshold is selected for our experiments on flat terrain. If necessitated by conditions such as uneven terrain, the static stability threshold may be raised to improve the capability of the robot to remain statically stable even when some modules fail to follow the prescribed contact states (e.g., perturbed by the environment).

3.1.4. Coordination of the horizontal and the vertical waves. We decomposed the internal shape of sidewinder robots into two independent traveling waves: a horizontal traveling wave and a vertical traveling wave. The horizontal traveling wave is prescribed by

$$\theta_l(j, \tau_1) = A_l \sin\left(2\pi K_l \frac{j}{N} + \tau_1\right) \quad (13)$$

where τ_1 is the phase of the horizontal wave. Similarly, the contact state is prescribed as

$$c(2i - 1, \tau_2) = c(2i, \tau_2) = \sigma\left(\sin\left(2\pi K_v \frac{i}{2N} + \tau_2\right)\right) \quad (14)$$

where τ_2 is the phase of the vertical wave that can uniquely determine the contact pattern. Here $c(i, \tau_2) = 0$ represents swinging state and, therefore, no ground reaction force appears at link i at phase τ_2 .

The phases of the horizontal wave and the vertical wave then comprise the shape variable, $\boldsymbol{\tau} = [\tau_1, \tau_2]^T$. Using the geometric mechanics gait design tools mentioned in Section 2, we can calculate the height function and visualize the kinematics in the desired directions (translational and rotational).

A gait that coordinates the horizontal and vertical wave can be described as a function that maps τ_1 to τ_2 . From the structure of the height functions (see Figure 2), we observed that in the Euclidean cover space of the torus (where the edges are properly identified with each other at 0 and 2π), a straight line-path gives rise to an optimal path; this is seen by the integral of the surface in the upper left minus the integral of the surface in the lower right being maximized. In this way, we characterize the coordination of the horizontal and the vertical wave by the relative phase lag: $\phi_0 := (\tau_2 - \tau_1 \bmod 2\pi)$.

3.2. Numerical simulation

We first performed numerical simulations to test our scheme's ability to predict locomotion. Specifically, in the simulation, we prescribed the horizontal amplitude and the contact state of the robot using (3) and (5). In other words, we take $\tau_1 = 2\pi ft$ and $\tau_2 = 2\pi f + \phi_0$. Thus, the shape variable and shape velocity can be prescribed as

$$\boldsymbol{\tau} = \begin{bmatrix} 2\pi ft \\ 2\pi ft + \phi_0 \end{bmatrix}, \quad \dot{\boldsymbol{\tau}} = \begin{bmatrix} 2\pi f \\ 2\pi f \end{bmatrix} \quad (15)$$

Then we simulate the locomotion with the standard ordinary differential equation (Hatton and Choset, 2015):

$$\begin{aligned} g(T) &= \int_0^T T_e L_{g(t)} A(\boldsymbol{\tau}) \dot{\boldsymbol{\tau}} dt \\ &= \int_0^T T_e L_{g(t)} A \left(\begin{bmatrix} 2\pi ft \\ 2\pi ft + \phi_0 \end{bmatrix} \right) \begin{bmatrix} 2\pi f \\ 2\pi f \end{bmatrix} dt \end{aligned} \quad (16)$$

where $g = (x, y, \alpha) \in SE(2)$ represents the body frame position and rotation (Murray, 2017),

$$T_e L_g = \begin{bmatrix} \cos(\alpha) & -\sin(\alpha) & 0 \\ \sin(\alpha) & \cos(\alpha) & 0 \\ 0 & 0 & 1 \end{bmatrix}$$

is the left lifted action with respect to the coordinates of g . Rate-independent kinetic Coulomb friction was used to derive the local connection matrix, A , where the ground reaction forces are related to the body velocity by

$$F^i = F_m \frac{v}{|v|} \quad (17)$$

where F^i is the ground reaction force experienced on the i th module, v is the body velocity, and F_m is the magnitude of the friction force.

Solving the differential equation 16 throughout one period (from $t=0$ to $t=1/f$), we obtain the trajectory of the locomotor and can, thus, determine the predicted displacements in the forward, lateral, and rotational directions over one gait cycle.

Note that we assume that the friction force dominates the motion and we neglect inertia in the simulation. However, inertia can be important in gait stability. That is, when the statically unstable gaits are implemented on robots with low temporal frequency (i.e., no dynamic stability), the robot often cannot reach the prescribed configuration; therefore, simulation–experiment discrepancy is expected (see Figure 5(a)). On the other hand, when operated at high temporal frequency, inertial effects can make the statically unstable gaits dynamically stable. In the case where the gait can be stably (either statically stable or dynamically stable) implemented on robots, inertia has a relatively small contribution to the motion (i.e., friction dominates the motion), as we show in Figure 5b.

3.3. SEA robot experiments

We conducted experiments with a SEA limbless robot (Figure 1(b)). Our SEA robot (mass 3.7 kg, length 1.2 m) is a modular series elastic actuated robot composed of a chain of 16 identical modules that are capable of precise torque, velocity, and position control (Rollinson et al., 2014). As described in Section 2.1, the arrangement of modules in the SEA robot ensures that the rotation axes of neighboring modules were 90° off along the longitudinal axis. Thus, the joints were divided into two groups: yaw joints (odd modules from head to tail), which control the

horizontal body wave, and pitch joints (even modules), which control the vertical body wave. Note that during the experiments, the connection wire was lifted to avoid the additional force.

Experiments were conducted on flat hard ground, where we assume the ground reaction forces are given by rate-independent kinetic Coulomb friction. The SEA robot was controlled directly by joint angle commands. For each sidewinder gait tested, we conducted five trials. In each trial, we commanded the SEA robot to execute two complete gait cycles and collected the SEA robot motion data starting from the first command being sent out until the SEA robot stop moving.

To track the motion of the SEA robot in the environment, we uniformly attached 17 infrared (IR) reflective markers along the body. An OptiTrack motion capture system was employed, and 4 OptiTrack Flex 13 cameras were installed to track the 3D positions of the markers at a frame rate of 120 frames per second (FPS). We recorded the trajectory of the markers over two cycles, from which we calculate the forward, lateral, and rotational displacements. Examples of the SEA robot experiments can be found in Extension 1.

We summarize our steps to stabilize the sidewinding gaits in Algorithm 1.

4. Results

4.1. Verification of CPR

In this subsection, we compare the locomotion performance using (3)–(4) (SWP) and the method introduced in Section 2.2 (CPR) to prescribe the joint angles. We compare three gaits: high stability (HS), intermediate stability (IS), and low stability (LS). The detailed parameters for these gaits are listed in Table 2. Note that in all three gaits, the expected rotation is zero with effective translational displacement (Astley et al., 2015; Rieser et al., 2019).

In the HS experiments, both methods can lead to almost no rotation with effective lateral displacements. This is as expected from previous experiments (Astley et al., 2015).

In the IS experiments, we note that there is significant body rotation in SWP, whereas in CPR, the body rotation is almost negligible. We hypothesize that SWP does not give accurate configurations as expected, which causes the discrepancy in contact patterns. To test our hypothesis, we measure the body contact and compare the empirically collected contact pattern data with the expectation given by (5). Interestingly, we observe that in SWP, the actual contact pattern in robot experiments (Figure 4(e2)) is clearly different from the expectation (Figure 4(e1)). In contrast, in CPR, the actual contact pattern in robot experiments (Figure 4(e3)) is almost identical to the expectation. Therefore, the discrepancy in contact pattern is at least one of the reasons for the unexpected turning in SWP robot experiments.

Finally, in the LS experiments, both methods display significant rotation. We suspect that this body rotation is

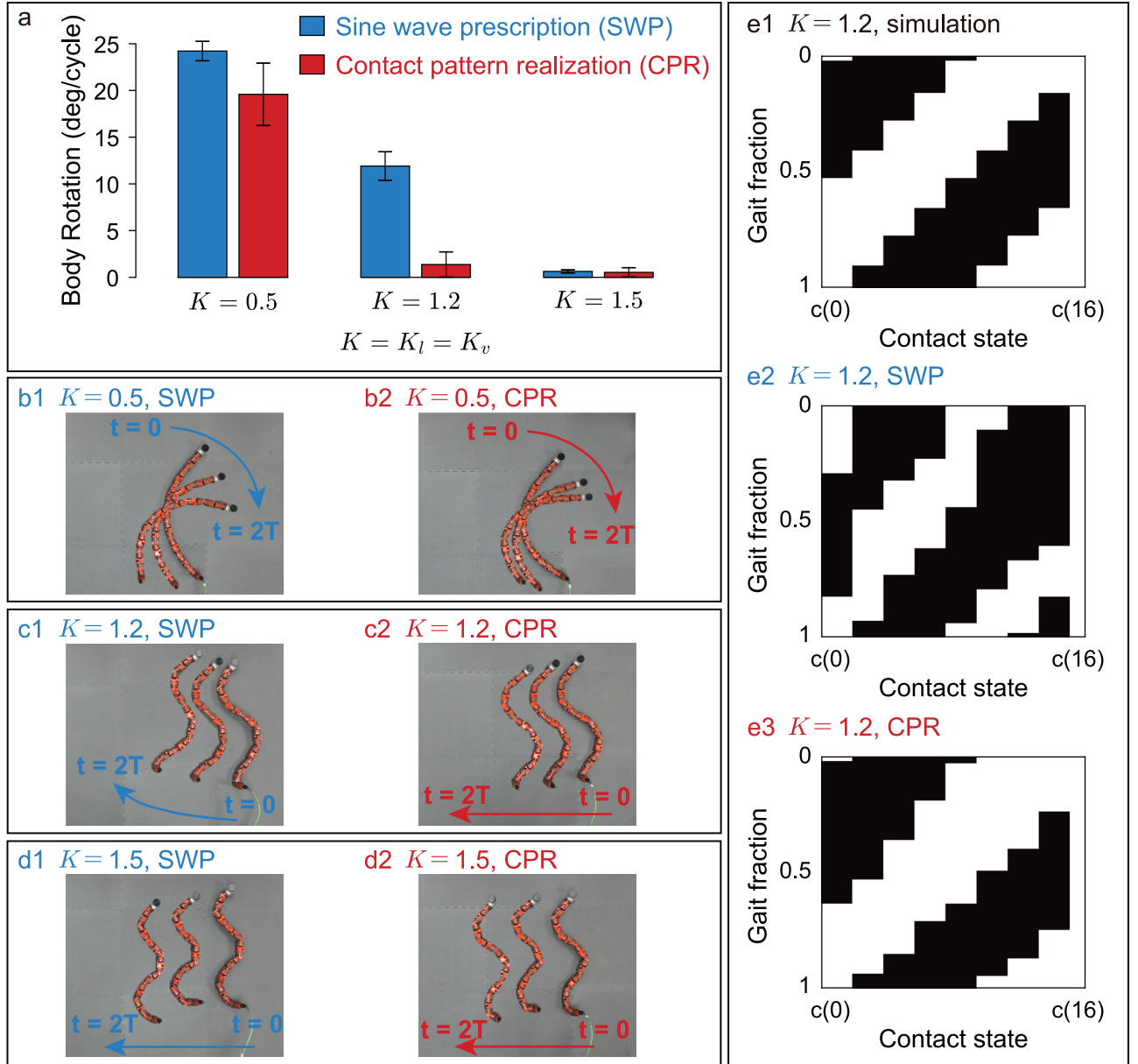


Fig. 4. Contact pattern comparison of the SWP (implementation of sine wave joint angle templates as in (3)–(4)) and the CPR method (introduced in Section 2.2). (a) Comparison of body rotations in low-stability (LS, $K = 0.5$), intermediate-stability (IS, $K = 1.2$), and high-stability (HS, $K = 1.5$) gaits. Both SWP and CPR cause low body rotations in the LS case and high body rotations in the HS case; in the IS case, significant body rotation is only observed in the SWP. (b)–(d) Snapshots of robot experiments implementing gaits using SWP (1) and CPR (2). (e) The comparison of IS body contact pattern from simulation (1), SWP (2), and CPR (3).

Table 2. Gait parameters for three sidewinding gaits: high stability (HS), intermediate stability (IS), and low stability (LS)

Gait	HS	IS	LS
K_l	1.5	1.2	0.5
K_l/K_v	1	1	1
A_l/K_l	0.7	0.7	0.7
A_v/K_v	0.15	0.15	0.15
ϕ_0	$\pi/2$	$\pi/2$	$\pi/2$
f	2.0	2.0	2.0
Stability	1.00	0.60	0.12

Algorithm 1: Stabilizing sidewinding and turning gaits

```

1 Initialization:  $K_v/K_l = 1.0$ ;
2 while Static Stability < 0.5 do
3    $K_v/K_l \leftarrow K_v/K_l + 0.1$ ;
4   CPR;
5   Calculate height function (HF);
6   Take  $\phi_0$  to maximize HF surface integral;
7 end
8 Perform numerical simulation
9 Implement robot experiments

```

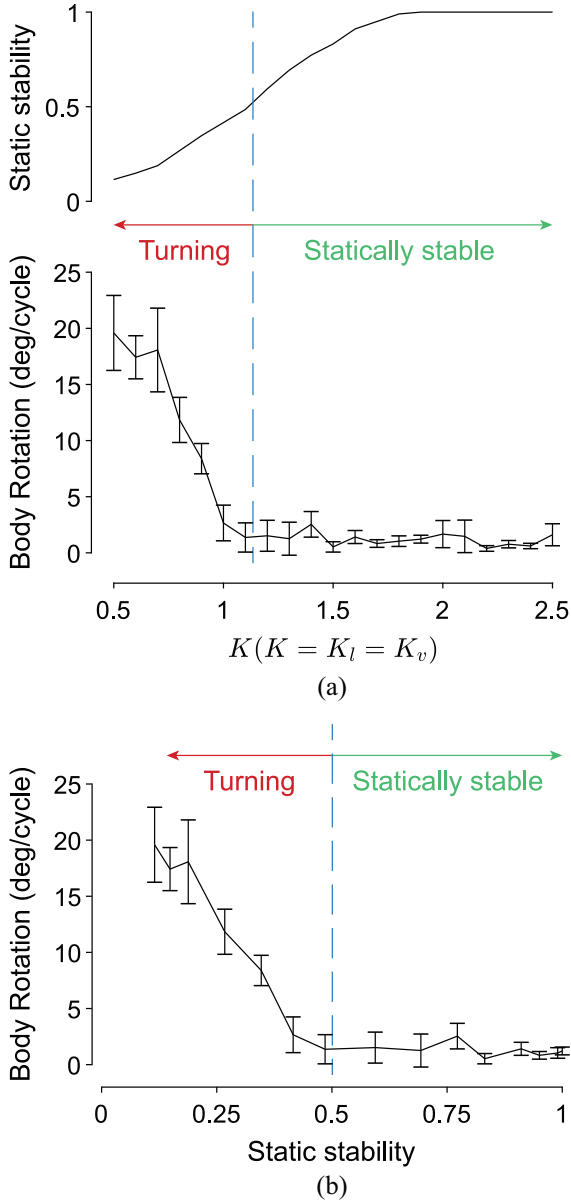


Fig. 5. Effect of spatial frequency on static stability. (a) The top panel shows the relationship between the spatial frequency ($K_v = K_l = K$) and the static stability. Robot experiments showed that significant turning (bottom panel) was observed in gaits with low static stability (top panel) and the turning vanished at gaits with high static stability. (b) We directly plotted the relationship between the body rotation and static stability. The curve appeared to be piecewise linear function. In the range where the static stability is less than 0.5, the body rotation grows almost linearly with the loss of static stability ($R^2 = 0.99$), whereas in the range where the static stability is higher than 0.5, the body rotation is almost negligible.

caused by the low stability contact pattern. We evaluate this in detail in later sections.

From the observations in this section, we have shown that contact pattern with at least intermediate static stability can be reliably realized using methods introduced in Section 2.2,

allowing us to directly modulate the contact pattern to stabilize gaits based on contact patterns prescribed by (5).

4.2. Statically unstable gaits

Previous work (Rieser et al., 2019) suggested that sidewinding gaits with 1.5 spatial waves ($K_l = 1.5$, $K_v/K_l = 1$) were typically faster than the sidewinding gaits with 2 spatial waves ($K_l = 2$, $K_v/K_l = 1$). In both cases, the gaits are statically stable and the simulation can predict the trajectory of body motion, with good agreement with experiments. With this knowledge, we proceed to study the locomotion performance of the statically unstable sidewinding gaits.

We calculate the static stability for sidewinding gaits with different spatial frequencies ($K_v = K_l = K$) in Figure 5. High spatial frequencies lead to a dense distribution of short contact patches (Figure 3(a)) and are often statically stable. In contrast, low spatial frequencies lead to sparse distribution of long contact patches (Figure 3(b)) and are often not statically stable.

To investigate the behavior of statically unstable sidewinding gaits, we perform similar experiments on sidewinding gaits with 0.9 spatial wave and 1.5 waves on our robot (Figure 1(b)). We set horizontal amplitude $A_l = 40K_l$ (unit of amplitudes: degrees), vertical amplitude $A_v = 8.5K_v$, and a temporal frequency $f = 2.0$ Hz for all the robot experiments unless otherwise stated. Snapshots of the robot implementing such gaits are shown in Figure 6. Good agreement between experiment and theory is observed in the sidewinding gait with 1.5 spatial waves. However, we observe significant discrepancies between the simulation and robot experiments the sidewinding gait with 0.9 spatial waves (see Figure 6). We hypothesize that at low spatial frequency, the configuration of the robot is not statically stable (static stability = 0.34 for 0.9 spatial wave, static stability = 0.83 for 1.5 spatial waves), which leads to the robot falling down (see Figure 3(b) and (c)) and causes contact patterns different from expectation. The unexpected touchdown can change the distribution of ground reaction forces and therefore lead to motions in other directions (in this case, turning).

We further conducted robot experiments across a range of spatial frequencies. Those robot experiments showed that such discrepancies (stability related turning) vanished at high spatial frequencies. We observed that, the cut-off static stability that leads to unexpected behavior is around 0.5. In this way, we use 0.5 as the threshold to determine the static stability in later analysis.

4.3. Temporal frequency dependency

Despite being statically stable, it is possible that, when operated at high temporal frequency, the acquired dynamic stability can compensate for the loss of static stability. Following this idea, we test the effect of the temporal frequency on the performance of gaits.

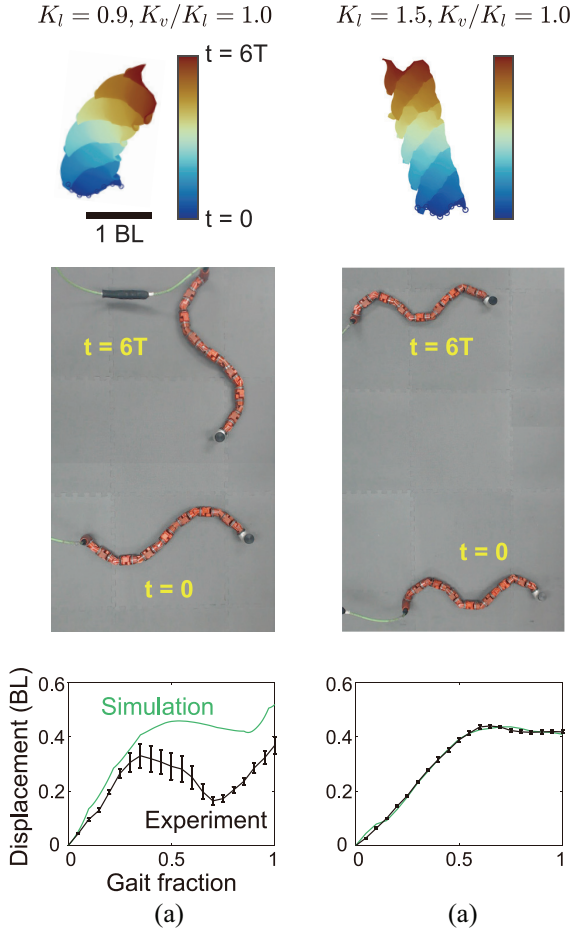


Fig. 6. Discrepancy between robot experiments and simulation at low spatial frequency. (Top) The trajectories of body motion in six gait cycles. The colors represent gait periods. Initial positions of the robot indicated by the black circles. (Bottom) Comparisons of time evolution of displacement of the simulation and robot experiments. We compared the low-spatial-frequency gait (a) and high-spatial-frequency gait (b). The simulation–experiment discrepancy occurs in low-spatial-frequency gaits. The unit and the axis labels in all panels are the same.

We first evaluate the effect of temporal frequency on the translational sidewinding gait with 0.9 spatial wave ($K_l = 0.9, K_v/K_l = 1$). We set $A_l = 50^\circ$ and $A_v = 75^\circ$ for all the SEA robot experiments. From our static stability analysis, this translational sidewinding gait is not statically stable (static stability = 0.35). At low temporal frequency (see Figure 7(a)), significant rotations are observed in robot experiments, whereas at high temporal frequency, the magnitude of rotation reduces but the robot rotates in a different direction. Our experiments show that the locomotion performance for statically unstable gaits is not predictable and controllable when operated at different temporal frequencies. However, the magnitude of rotation significantly decreases when the SEA robot was operated at high temporal frequency, which suggests that the loss of static stability can be compensated by emergent dynamic stability at high speed.

Next, we evaluate the temporal frequency dependence of the rotational sidewinding gait from Astley et al. (2015): $K_l = 1.5, K_v/K_l = 0.6$, and $\phi_0 = \pi/2$. From our static stability analysis, the rotational sidewinding gait is not statically stable (static stability = 0.46). In addition, numerical simulation predicts that the rotational sidewinding gaits should lead to counterclockwise rotation, in contrast with the results in Astley et al. (2015). Therefore, we suspect that the rotational sidewinding gait is driven by the unexpected touchdowns and, therefore, will be strongly temporal frequency dependent. SEA robot experiments verified that locomotion performance (Figure 7(b)) in the rotational sidewinding gait is strongly correlated with the temporal frequency. Higher rotation angles are achieved when the SEA robot operated at low temporal frequency.

4.4. Stabilization by contact modulation

We use the algorithms proposed in Section 3 to stabilize the statically unstable translational and rotational sidewinding gaits. As discussed previously, the translational sidewinding gait with 0.9 spatial wave is not statically stable. We show that we can stabilize this gait by increasing the V – L ratio K_v/K_l to 1.2. From the lateral height function (Figure 2(b)), we take $\phi_0 = 1.076$ to optimize the surface enclosed in the lateral height function. The static stability analysis suggests that this gait is statically stable (static stability = 0.5). We implement this gait on SEA robot experiments (Figure 8(a)), which show that no significant turning was observed over our range of temporal frequencies.

Note that the stabilized translational sidewinding gait ($K_l = 0.9, K_v/K_l = 1.2$) exhibited effective lateral displacement. SEA robot experiments demonstrate that the average lateral displacement per gait cycle is 0.69 ± 0.02 body lengths per cycle, significantly greater than the displacement (0.42 ± 0.01 body length per gait cycle) of the translational sidewinding gait with 1.5 spatial waves ($K_l = 1.5, K_v/K_l = 1$).

We next stabilize the rotational sidewinding gait with 1.5 spatial waves, $K_l = 1.5$. We show that we can stabilize this gait by raising the V – L ratio K_v/K_l to 1.3. From the rotational height function (Figure 2(a)), we take $\phi_0 = 1.02$ to optimize the surface enclosed in the rotational height function. The static stability analysis suggests that this gait is statically stable (static stability = 0.62). We implement this gait on the SEA robot (Figure 8(b)), revealing that the locomotion performance (rotation per gait cycle) is robust over a range of temporal frequencies.

4.5. General sidewinding gait formula

4.5.1. Empirical sidewinding governing equation. As discussed earlier, the coordination pattern of horizontal and vertical waves in sidewinding locomotion has been well studied and documented (Astley et al., 2015, 2020; Burdick et al., 1993; Hu et al., 2009; Marvi et al., 2014; Rieser et al., 2019). Some of the well-known sidewinding gaits are

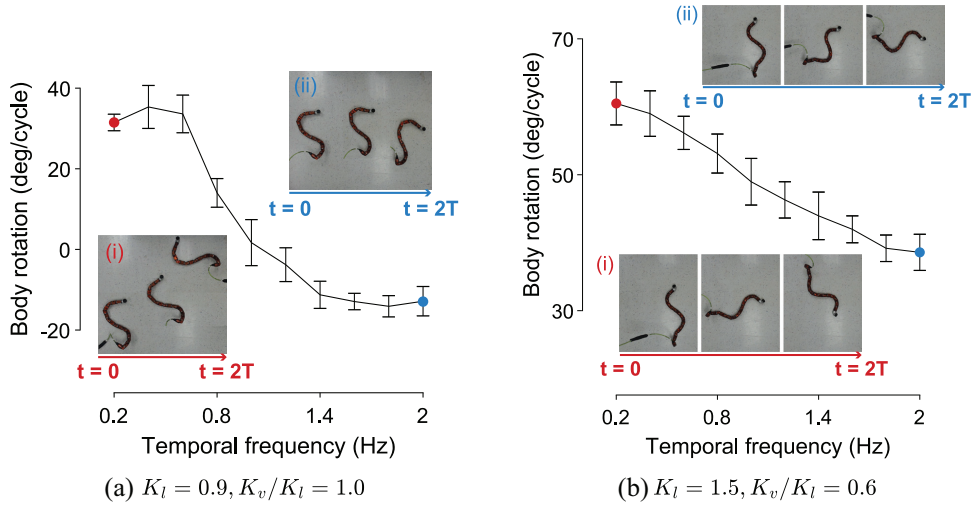


Fig. 7. Temporal frequency dependency of unstable gaits. Dependence of the rotation angle (per cycle) on the temporal frequency of (a) statically unstable translational sidewinding gaits and (b) statically unstable rotational sidewinding gaits on SEA robot experiments. The subplots (i) and (ii) show the snapshots of the SEA robot implementing gaits in low temporal frequency (0.2 Hz, red) and high temporal frequency (2.0 Hz, blue) over three gait cycles.

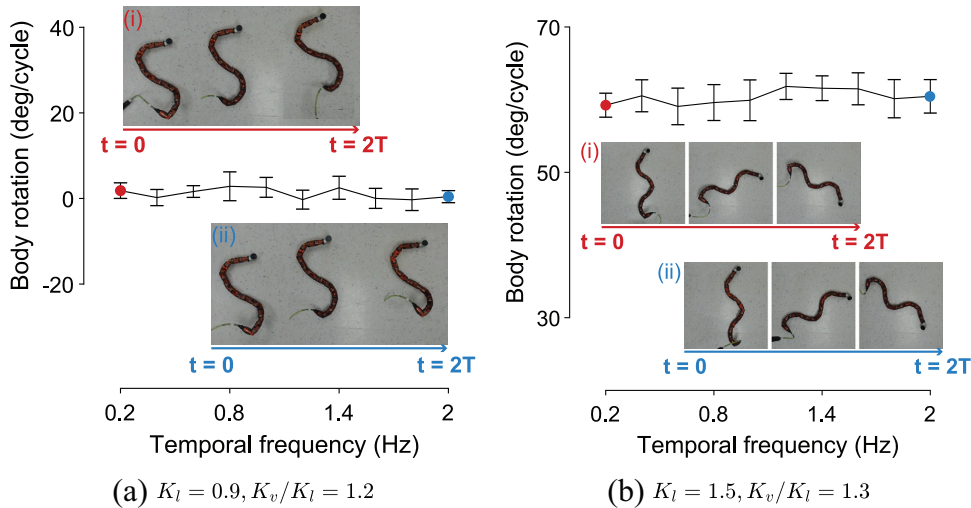


Fig. 8. Robustness of statically stable gaits as a function of temporal frequency. Dependence of the rotation angle (per cycle) on the temporal frequency of (a) the stabilized translational sidewinding gaits and (b) the stabilized rotational sidewinding gaits on SEA robot experiments. In both cases, the rotation angle is steady over a range of temporal frequencies. The unit and the axis labels in all panels are the same. The subplots (i) and (ii) show the snapshots of the SEA robot implementing gaits in low temporal frequency (0.2 Hz, red) and high temporal frequency (2.0 Hz, blue) over three gait cycles.

summarized in Table 1. In previous sections, we showed that there is a broad range of gait parameters that can produce pure translation or pure rotation. In this section, we explore the question of whether empirical equations governing sidewinding gait parameters exist and can be identified. Such equation can help us better understand the kinematic principles behind the seeming complex sidewinding motion.

First, we show in Figure 9(a) that when we fix the horizontal spatial frequency K_l and modulate the $V-L$ ratio, the

patterns of height functions change accordingly. Surprisingly, we note that the emerging ϕ_0 linearly correlates with the $V-L$ ratio K_v/K_l , with slope $a = -0.44$ and intercept $b = 1.2$ ($R^2 = 0.96$). We then investigate how the slope and intercept are related to the horizontal spatial frequency K_l . From Figure 9(b), we see that both slope a and intercept b linearly correlate with K_l . Therefore, we can formulate an empirical function that governs the sidewinding gait parameters for the pure sideways translational motion ($R^2 = 0.98$):

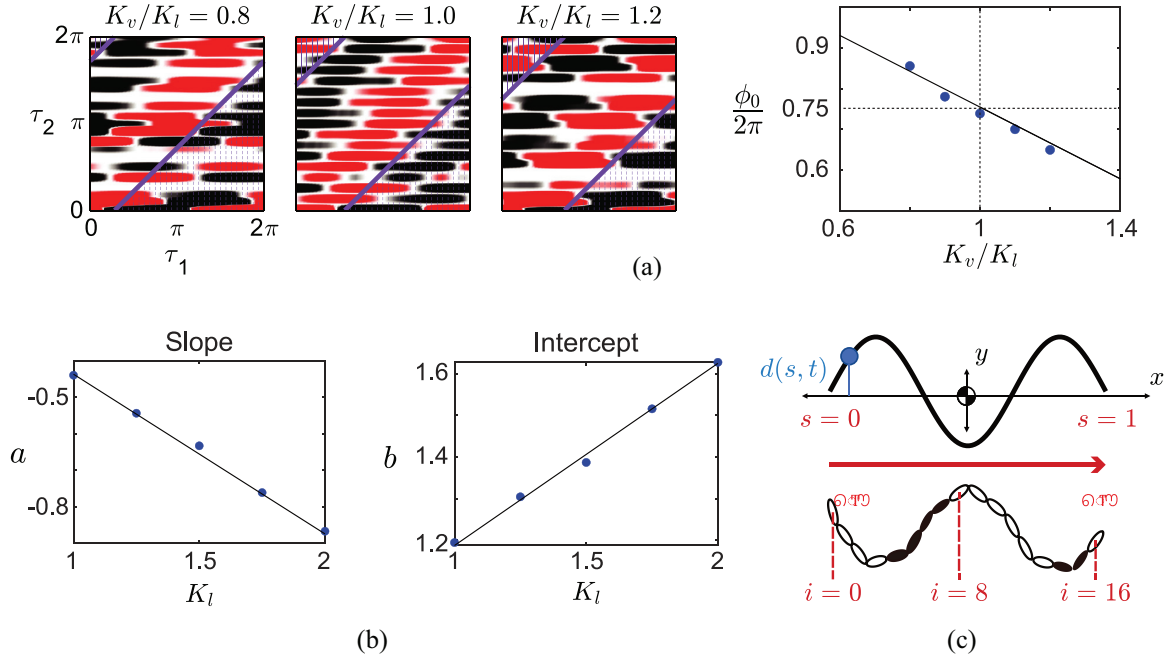


Fig. 9. Extended sidewinding gait formula. (a) Height functions for different $V-L$ ratios with fixed $K_l = 1.0$. We showed that while we change the $V-L$ ratio, the optimal phase ϕ_0 emerged to increase linearly from height function predictions. We then ran regression and we do find that $\phi_0/2\pi$ linearly correlates with $V-L$ ratio K_v/K_l , under slopes $a = -0.44$ and intercept $b = 1.2$. (b) We then test how the slopes and intercept correlates with the horizontal spatial frequency K_l . It turns out that both the slope a and the intercept b linearly correlate with K_l ($a \sim -0.439K_l + 0.001$, $b \sim 0.439K_l + 0.750$). (c) A model to explain the empirical equations. We develop our model in CoM frame, neglecting the forward displacement (along the direction) of body segments, and only investigate the effect of lateral displacement.

$$\frac{\phi_0}{2\pi} = -0.438(K_v - K_l) + 0.750 \quad (18)$$

Similarly, we can obtain the empirical equation that governs the sidewinding gait parameters for backwards translation (enables pure sideways translation in the opposite direction to the motion enabled by (18), $R^2 = 0.98$):

$$\frac{\phi_0}{2\pi} = -0.438(K_v - K_l) + 0.250 \quad (19)$$

CW in-place turning (maximal area in rotation height function, $R^2 = 0.98$)

$$\frac{\phi_0}{2\pi} = -0.438(K_v - K_l) + 0.498 \quad (20)$$

and counterclockwise in-place turning (minimal area in rotation height function, $R^2 = 0.98$)

$$\frac{\phi_0}{2\pi} = -0.438(K_v - K_l) + 0.001 \quad (21)$$

4.5.2. Simple model for sidewinding governing equations. In this section, we develop a model to derive the conditions for sidewinding gaits that exhibit T-sidewinding and R-sidewinding.

Consider a continuous traveling wave (Figure 9(c)) in the CoM frame. The lateral displacement of a body segment can be expressed as $d(s, t) = d_m \sin(\omega t - 2\pi K_l s)$, where

d_m is the amplitude of undulation. Its non-swinging-state spans the period

$$\{t | t \in [\phi_0 + 2\pi K_v s, \phi_0 + 2\pi K_v s + \pi]\}$$

To simplify the derivation, we use a linear expression $F = \beta v$ to model the ground reaction force instead of the discontinuous Coulomb friction. Although this linear expression differs from the Coulomb friction (see (17)), it can at least offer reasonably good local approximations, especially when v is small (Selmic and Lewis, 2002). In addition, the linear expression can also allow us to study the kinematics analytically. In this way, the ground reaction force can be calculated as

$$F(s, t) = \beta \frac{\partial d(s, t)}{\partial t} = f_m \cos(\omega t - 2\pi K_l s)$$

where f_m is the amplitude of ground reaction force. Then we can calculate the angular momentum contribution (with respect to CoM frame) at position s over a period as

$$\begin{aligned} L(s) &= \int_{\phi_0 + 2\pi K_v s}^{\phi_0 + 2\pi K_v s + \pi} \left(s - \frac{1}{2}\right) f_m \cos(\omega t - 2\pi K_l s) \\ &= L_m \left(s - \frac{1}{2}\right) \sin(\phi_0 + 2\pi s(K_v - K_l)) \end{aligned}$$

where L_m is the amplitude of angular momentum. We then propose a sufficient condition for pure translation without rotation in locomotion as $L(s) + L(1-s) = 0$, meaning that

the angular momentum contributions from two body segments symmetric about the CoM cancel. Solving for $L(s) + L(1 - s) = 0$, we obtain

$$\frac{\phi_0}{2\pi} = -\frac{1}{2}(K_v - K_l) + \frac{1}{4} + \frac{1}{2}k$$

where $k \in \mathbb{Z}$.

In the discrete case, where in a N -link robot (or a $(N - 1)$ -joint robot, N as an odd number), the central link is located at $i = \frac{N-1}{2}$, therefore the governing equation should be modified to

$$\frac{\phi_0}{2\pi} = -\frac{N-1}{2N}(K_v - K_l) + \frac{1}{4} + \frac{1}{2}k \quad (22)$$

In our case, $N = 17$, the analytic equation ((22)) and empirical equation ($k = 1$ for (18) and $k = 0$ for (19)) are close in numerical values.

Similar to the pure translation without rotation situation, the maximal CW/counterclockwise in-place rotation situation can be expressed as $L(s) = L(1 - s)$, where the angular momentum contribution from two body segments symmetric to CoM have the same direction. Solving for $L(s) = L(1 - s)$, we can obtain the continuous case

$$\frac{\phi_0}{2\pi} = -\frac{1}{2}(K_v - K_l) + \frac{1}{2}k$$

and discrete condition

$$\frac{\phi_0}{2\pi} = -\frac{N-1}{2N}(K_v - K_l) + \frac{1}{2}k \quad (23)$$

where $k \in \mathbb{Z}$. Note that, in our case, $N = 17$, thus (23) are close to the empirical equations ($k = 1$ for (20) and $k = 0$ for (21)).

5. Discussion

5.1. Sidewinding gait family

In previous work, T-sidewinding gaits were described as the superposition of body waves in the horizontal and the vertical planes of the same spatial frequency ($K_v = K_l$). This equality limited the applicability of sidewinding gaits, especially at low temporal frequency. In this work, we showed that $K_v = K_l$ is not necessary to produce translational sidewinding locomotion. In fact, for almost any $V-L$ ratio, K_v/K_l , we can always find a ϕ_0 to produce pure translation.

In our expanded sidewinding gait family, smaller $V-L$ ratio in general corresponds to faster but less-stable locomotion; greater $V-L$ ratio, in general, corresponds to slower but more stable gaits. By modulating the $V-L$ ratio, we can systematically tune the balance between the speed and stability.

5.2. Mechanisms of frequency turning gaits

Turning motions of limbless robots have been less studied than translational motion. R-sidewinding (also known as frequency turning in Astley et al. (2015), modulating the

$V-L$ ratio with fixed phase lag $\phi_0 = \pi/2$) was identified as an effective in-place turning strategy for limbless locomotors (Astley et al., 2015). However, the mechanism of frequency turning gaits was not well understood.

In this article, we studied frequency turning gaits systematically. Static stability analysis shows that the frequency turning gaits with $V-L$ ratio greater than one are statically stable. Moreover, SEA robot experiments showed that the locomotion performance of frequency turning gaits with $V-L$ ratio greater than one was not temporal frequency dependent. Our kinematic model suggested that it is the changes in the symmetry of ground reaction forces that lead to the changes in the direction of motion.

On the other hand, in the simulation and geometric mechanics prediction, the frequency turning gaits should lead to counterclockwise turning when the $V-L$ ratio is less than one, which contradicts the experimental results. Furthermore, static stability analysis shows that the frequency turning gaits with $V-L$ ratio less than one are not statically stable. SEA robot experiments also suggested that their locomotion performances are not robust over the temporal frequencies. In this way, we speculate that the frequency turning gaits with $V-L$ ratio less than one are driven by the unexpected ground reaction forces in the unstable configurations.

6. Conclusion

In this article, we have shown that, at low temporal frequency, statically unstable sidewinding gaits have undesirable locomotion performance and deviate from simulation expectations. In other words, these unstable gaits are predictable only at high temporal frequency, where the static instability can be compensated for by the gained dynamic stability. In fact, the loss of static stability limits the feasible choices of sidewinding gaits at low temporal frequency.

We have proposed an approach to stabilize these statically unstable sidewinding gaits by modulating the spatial frequency of the vertical wave. We have used height functions, analytic tools previously developed in the geometric mechanics literature, to coordinate the horizontal wave and vertical wave to produce effective motion in the desired directions. Robot experiments have verified that the temporal frequency dependence was eliminated in stabilized sidewinding gaits.

In this way, we have greatly expanded the range of statically stable sidewinding gaits by introducing another control variable K_v/K_l to regulate the trade-off between the static stability and the speed (temporal frequency). Limbless robots in the real world should not only achieve effective locomotive performances at high speed but also locomote stably at low speed. For example, in the scenario of snake robots navigating through cluttered environments for search and rescue, stability is often more important than the speed. Hence, our method expands the range of statically stable sidewinding gaits and extends the applicability

of limbless robots to those environments where being operated in high temporal frequency is not possible. Our work can also generate testable neuromechanical control hypotheses for how living systems coordinate multiple body waves to translate or rotate stably and/or rapidly.

Acknowledgments

We would like to thank Christopher J. Pierce for helpful discussions and proofreading.

Funding

The author(s) disclosed receipt of the following financial support for the research, authorship, and/or publication of this article: This paper was supported by NSF PoLS PHY-1205878 and ARO W911NF-11-1-0514.

ORCID iDs

Baxi Chong  <https://orcid.org/0000-0002-6187-4911>
 Tianyu Wang  <https://orcid.org/0000-0001-9012-838X>
 Bo Lin  <https://orcid.org/0000-0001-9120-3142>

References

- Astley HC, Gong C, Dai J, et al. (2015) Modulation of orthogonal body waves enables high maneuverability in sidewinding locomotion. *Proceedings of the National Academy of Sciences* 112(19): 6200–6205.
- Astley HC, Mendelson JR, Dai J, et al. (2020) Surprising simplicities and syntheses in limbless self-propulsion in sand. *Journal of Experimental Biology* 223(5): jeb103564.
- Burdick JW, Radford J and Chirikjian GS (1993) A ‘sidewinding’ locomotion gait for hyper-redundant robots. In: *Proceedings IEEE International Conference on Robotics and Automation*, IEEE, pp. 101–106.
- Chong B, Aydin YO, Sartoretti G, et al. (2019) A hierarchical geometric framework to design locomotive gaits for highly articulated robots. In: *Proceedings of Robotics: Science and Systems*.
- Fu Q and Li C (2020) Robotic modelling of snake traversing large, smooth obstacles reveals stability benefits of body compliance. *Royal Society Open Science* 7(2): 191192.
- Gong C, Travers M, Astley HC, Goldman DI and Choset H (2015) Limbless locomotors that turn in place. In: *2015 IEEE International Conference on Robotics and Automation (ICRA)*. IEEE, pp. 3747–3754.
- Gong C, Whitman J, Grover J, Chong B, Ren R and Choset H (2018) Geometric motion planning for systems with toroidal and cylindrical shape spaces. In: *Proceedings of the Dynamic Systems and Control Conference*.
- Hatton RL and Choset H (2010) Sidewinding on slopes. In: *2010 IEEE International Conference on Robotics and Automation*. IEEE, pp. 691–696.
- Hatton RL and Choset H (2015) Nonconservativity and noncommutativity in locomotion. *The European Physical Journal Special Topics* 224(17–18): 3141–3174.
- Hatton RL, Ding Y, Choset H and Goldman DI (2013) Geometric visualization of self-propulsion in a complex medium. *Physical Review Letters* 110(7): 078101.
- Hu DL, Nirody J, Scott T and Shelley MJ (2009) The mechanics of slithering locomotion. *Proceedings of the National Academy of Sciences* 106(25): 10081–10085.
- Ijspeert AJ, Crespi A, Ryzcko D and Cabelguen JM (2007) From swimming to walking with a salamander robot driven by a spinal cord model. *Science* 315(5817): 1416–1420.
- Jayne BC (1986) Kinematics of terrestrial snake locomotion. *Copeia* 4: 915–927.
- Kobayashi S and Nomizu K (1963) *Foundations of Differential Geometry*, Vol. 1. New York: Interscience.
- Li C, Umbanhowar PB, Komsuoglu H, Koditschek DE and Goldman DI (2009) Sensitive dependence of the motion of a legged robot on granular media. *Proceedings of the National Academy of Sciences* 106(9): 3029–3034.
- Lin B, Chong B, Ozkan-Aydin Y, et al. (2020) Optimizing coordinate choice for locomotion systems with toroidal shape spaces. In: *2020 IEEE/RSJ International Conference on Intelligent Robots and Systems (IROS)*, pp. 7501–7506.
- Marsden JE and Ratiu TS (2013) *Introduction to Mechanics and Symmetry: A Basic Exposition of Classical Mechanical Systems*, Vol. 17. Springer Science & Business Media.
- Marvi H, Gong C, Gravish N, et al. (2014) Sidewinding with minimal slip: Snake and robot ascent of sandy slopes. *Science* 346(6206): 224–229.
- MATLAB (2020) *version 9.8.0 (R2020a)*. Natick, MA: The MathWorks Inc.
- McGeer T (1990) Passive dynamic walking. *The International Journal of Robotics Research* 9(2): 62–82.
- McGhee RB and Iswandhi GI (1979) Adaptive locomotion of a multilegged robot over rough terrain. *IEEE Transactions on Systems, Man, and Cybernetics* 9(4): 176–182.
- Murray RM (2017) *A Mathematical Introduction to Robotic Manipulation*. Boca Raton, FL: CRC Press.
- Pongas D, Mistry M and Schaal S (2007) A robust quadruped walking gait for traversing rough terrain. In: *Proceedings 2007 IEEE International Conference on Robotics and Automation*. IEEE, pp. 1474–1479.
- Ponton B, Khadiv M, Meduri A and Righetti L (2020) Efficient multi-contact pattern generation with sequential convex approximations of the centroidal dynamics. *arXiv preprint arXiv:2010.01215*.
- Rieser JM, Gong C, Astley HC, et al. (2019) Geometric phase and dimensionality reduction in locomoting living systems. *arXiv preprint arXiv:1906.11374*.
- Rollinson D, Bilgen Y, Brown B, et al. (2014) Design and architecture of a series elastic snake robot. In: *2014 IEEE/RSJ International Conference on Intelligent Robots and Systems*. IEEE, pp. 4630–4636.
- Selmic RR and Lewis FL (2002) Neural-network approximation of piecewise continuous functions: Application to friction compensation. *IEEE Transactions on Neural Networks* 13(3): 745–751.
- Takemori T, Tanaka M and Matsuno F (2018) Ladder climbing with a snake robot. In: *2018 IEEE/RSJ International Conference on Intelligent Robots and Systems (IROS)*. IEEE, pp. 1–9.
- Wang T, Lin B, Chong B, et al. (2021) Reconstruction of backbone curves for snake robots. *IEEE Robotics and Automation Letters* 6(2): 3264–3270.
- Zhong B, Aydin YO, Gong C, et al. (2018) Coordination of back bending and leg movements for quadrupedal locomotion. In: *Proceedings of Robotics: Science and Systems*.

Appendix. Index to multimedia extensions

Archives of IJRR multimedia extensions published prior to 2014 can be found at <http://www.ijrr.org>, after 2014 all videos are available on the IJRR YouTube channel at <http://www.youtube.com/user/ijrrmultimedia>

Table of Multimedia Extensions

Extension	Media type	Description
1	Video	Examples of the SEA robot experiments